PAPER

Check for updates

Bio-mimicking TiO$_2$ architectures for enhanced photocatalytic activity under UV and visible light†

Iman Hashemizadeh,[a] Daniel C. W. Tsang, [ID] [b] Yun Hau Ng, [ID] [cf] Zhijie Wu,[d] Vladimir Golovko [ID] *[e] and Alex C. K. Yip*[af]

Green leaves are responsible for natural photosynthesis in plants and their unique structures offer the most efficient blueprint for artificial materials in terms of solar energy capture and utilisation. The full architecture of the leaf photosystem was successfully replicated at both the nano and micro levels using biotemplating with TiO$_2$. This approach resulted in a highly porous structure that can be used as a photocatalyst with enhanced properties such as improved visible light-harvesting ability. Scanning and transmission electron microscopy images of the final products confirmed that the detailed microscale framework and nanostructures, such as the chloroplast and the thylakoids were well replicated. Biotemplated artificial TiO$_2$ leaves with the architecture of *Camellia* tree leaves outperformed well-known P25 TiO$_2$ in photocatalytic degradation of methylene blue dye under visible light: more than twofold in the case of blue (440 nm) and *ca.* one and a half times under green (515 nm) light. Also, the carbon dioxide yield of photocatalytic oxidation of ethanol catalysed by the biotemplated TiO$_2$ material was approximately 1.3 times higher than the CO$_2$ produced by P25 under green light. We attributed this enhanced visible light photocatalytic performance to the light-harvesting features and to the high surface area imparted by the interconnected nanosheets (replicating the thylakoids) resulting from our improved biotemplating method. The method reported in this work presents a facile route for the production of synthetic inorganic materials which possess morphologies similar to that present in the natural template materials.

1 Introduction

The efficiency of solar-assisted reactions strongly depends on the activity of the photocatalysts. Semiconductors possess a band structure in which the conduction band is separated from the valence band by a band gap with a suitable width for the absorption of photons. When the energy from incident light is greater than that of the band gap, electron hole pairs are formed.[1–4] Currently, more than 130 materials and derivatives are known to function as photocatalysts, including simple metal oxides, niobates, tantalates, metal nitrides, metal sulphides and covalent network solids such as C$_3$N$_4$. Among all of these materials, titanium dioxide (TiO$_2$)-based photocatalysts have been considered as one of the best materials due to their wide availability, low toxicity, good durability, high stability and, most importantly, favourable energies of photogenerated electrons and holes, which results in high photocatalytic efficiency.[5–7]

A vast range of TiO$_2$ structures, including nanosheets, nanowires, nanotubes, and hierarchical architectures, have been developed to improve both light harvesting efficiency and visible light photocatalytic activity *via* structuring of titania.[8–13] Commonly studied nanoscale TiO$_2$ can be synthesised *via* a number of different methods, including sol–gel, micellar and solvothermal syntheses, direct oxidation, chemical or physical vapour deposition, electrodeposition or anodization, and microwave synthesis.[14] The sol–gel method is widely used to produce small, well-defined particles even at relatively low temperatures. This method also enables the introduction of secondary components (*e.g.*, active metals) into the reaction mixture, which allows the synthesis of application-oriented TiO$_2$-based materials.[15] Although titanium tetrachloride (TiCl$_4$) was used as a precursor in the initial studies of TiO$_2$ synthesis, this

[a]Department of Chemical and Process Engineering, University of Canterbury, Christchurch, New Zealand. E-mail: alex.yip@canterbury.ac.nz

[b]Department of Civil and Environmental Engineering, Hong Kong Polytechnic University, Hong Kong, China

[c]School of Chemical Engineering, University of New South Wales, Australia

[d]State Key Laboratory of Heavy Oil Processing, The Key Laboratory of Catalysis of CNPC, China University of Petroleum, Beijing, 102249, China

[e]Department of Chemistry, University of Canterbury, Christchurch, New Zealand. E-mail: vladimir.golovko@canterbury.ac.nz

[f]The Joint Laboratory for Energy and Environmental Catalysis, City University of Hong Kong, Hong Kong, China

† Electronic supplementary information (ESI) available: Chloroplast isolation procedure, results of the dye degradation experiments without irradiation, XRD pattern of the non-coated Ti^{3+} exchanged samples, energy-dispersive X-ray spectroscopy (EDS) measurements, nitrogen adsorption–desorption isotherm, elemental surface composition of the MNAL, normalized results of methylene blue dye degradation, results of the total organic carbon (TOC) measurements and estimation of apparent kinetic constants of methylene blue dye degradation. See DOI: 10.1039/c7ra04185c

approach resulted in the formation of chloride ions as impurities in the product. Recent synthetic methods have focused on the use of titanium alkoxides, $Ti(OR)_4$, where R is an alkyl group, as precursors. The precursor is dissolved in water or in a mixture of solvents and is hydrolysed to give $Ti(OH)_xR_{4-x}$, which subsequently undergoes condensation through either substitution or addition reactions to produce TiO_2. Both halide and alkoxide compounds of titanium hydrolyse rapidly in the presence of water, causing difficulty in controlling the end product. Thus, post-synthesis modifications are necessary for tuning the properties of the end product. The most common technique is to use a solution containing acids and alcohol, in which the former serve as a catalyst and peptising agent. The use of alcohol as a solvent, on the other hand, can substantially reduce the temperature required in the TiO_2 synthesis process.[16,17] However, using structural facilitating agents to control the shape, size and crystallinity of the end product still remains as a challenge. For example, the use of fluoride and other fluorine-containing ions to control the particle shape of TiO_2 often results in surface-bound fluorine in the end product, which negatively influences the photocatalytic properties of TiO_2.[18,19]

Recently, bio-inspired materials have emerged as a potential area of research for developing advanced functional systems with a higher standard of environmental compatibility, recyclability and energy efficiency.[20] Natural materials offer a combination of advantageous properties, such as sophistication, miniaturization, hierarchical organization, hybridization, resistance and adaptability, which have evolved through billions of years of the natural selection processes. The morphologies of the biological structures ranging from the nanometre to the millimetre scale inspire the design of artificial materials that aim at advanced applications, such as energy capture, storage and conversion.[21,22]

Many bio-mimicking methods have recently been developed, including the following approaches:

(a) Replication, which involves use of biological templates to replicate the morphology *via* chemical transformations or physical processes, such as nanocasting and nanolithography;

(b) Self-assembly, which relies on using biological systems (usually at the nanoscale) as building blocks for a controllable assembly into complex structures through electrostatic, metal–ligand and inter-biomolecular interactions;

(c) Encapsulation, whereby biomolecules or living cells are isolated from their superstructures and encapsulated into man-made matrices with complex structures to form bioreactors.[22,23]

The templating method has recently emerged as an effective approach to overcome the difficulty in controlling the morphology of the end product.[24–26] The main advantage of this technique is that the final structure can be easily tuned through selection of a template with an appropriate morphology. By contrast, the conventional sol–gel synthesis is strongly affected by the conditions of the synthesis, including the pH of the solution, drying, subsequent thermal treatments *etc.* Importantly, controlled self-assembly of the primary nanoparticulate building blocks into larger-scale structures is a major challenge in this case. In efforts to develop TiO_2-based photocatalysts with improved light-harvesting functions, researches have recently
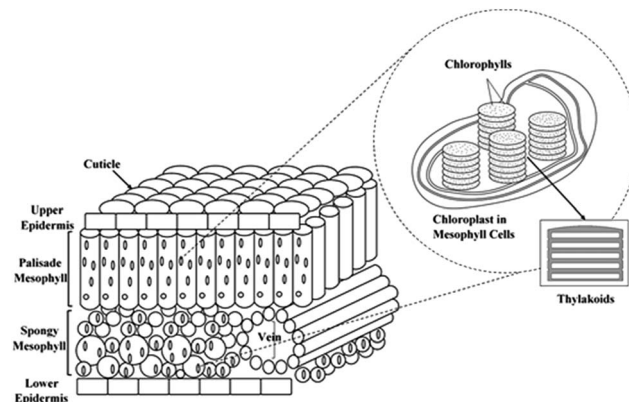

Fig. 1 The microscale-to-nanoscale structures of leaf photosystem.

proposed a few biotemplating techniques for reproduction of the natural hierarchical structures.[16,27–29] However, further research on the details of the biotemplating process and the relationship between the morphology of obtained product and its photocatalytic performance is required.

The photosystem of the green leaves naturally evolved both at the molecular level and at the structural level (nanoscale and microscale frameworks), making it overall a superior light-harvesting structure.[23,30] The lens-like epidermal cells focus incident light, and cylinder cells of palisade parenchyma serve as channels for the focused light, where the channels are arranged parallel to the incident light direction. The less-regular arrangement of spongy mesophyll leads to light scattering and long effective light path lengths in the intercellular air spaces of the leaf.[31–34] Although such complex porous architectures trap sunlight within the leaves, the main antenna of plants' photosystem is the chloroplast. The thylakoid cylindrical stacks (granum) inside the chloroplast are 3-dimensional scaffolds made of interconnected nanolayers. These structures harvest the light efficiently by directing the sunlight to the chlorophyll molecules which are the reactive centres of the plant photochemical machine.[35–37] The overall structure of the leaf photosystem is schematically illustrated in Fig. 1.

In this research, the structure of *Camellia sinensis* tree leaves from the family Theaceae, belonging to C_4 plants possessing the Kranz anatomy, has been replicated using TiO_2 from the microscale to the nanoscale. The photocatalytic activity of the artificial TiO_2 leaves at different level of biomimicked structures was studied through methylene blue degradation and the photocatalytic oxidation of ethanol under UV and visible light irradiation. We aim to demonstrate that presence of the structures analogous to the stack-layered nanostructures and mesoporous architectures present in natural leaves offer a unique opportunity for efficient use of novel TiO_2 structures under visible light.

2 Experimental

2.1 Materials

All reagents were of analytical grade and were purchased from Sigma-Aldrich. Methylene blue was supplied by Sekolah Tinggi Teknologi Tekstil, Indonesia. All reagents were used as received.

All glassware was oven dried and experiments were performed using Schlenk line technique to avoid contact with ambient air when required.

2.2 Synthesis procedure of bio-mimicked TiO$_2$ architectures

The replication of nano- to micro-architectures of leaf photosystem was done by ion-exchange method to mimic the natural chlorophyll breakdown process. Fresh leaves were first washed with MilliQ water, dried and cut into *ca.* 2 by 2 cm pieces. Then, 2.00 g of cut leaves was acid treated with a 5 v/v% HCl solution under inert atmosphere (Schlenk line technique) with vigorous stirring (250 rpm) using magnetic stirrer at room temperature for 3 h until the leaves changed the colour to yellow-brown. Ion-exchange was subsequently carried out in a 5 v/v% TiCl$_3$ solution in water with stirring (250 rpm) under inert atmosphere at ambient temperature overnight. The Ti^{3+} exchanged leaves were then coated with titania using a sol–gel approach modified from the previously reported method.[38] The treated leaves were collected on the Büchner funnel, washed with MilliQ water (3 × 50 mL) and dried in the vacuum desiccator over P$_2$O$_5$. Resulting dry leaves were suspended with stirring (250 rpm) in dry isopropanol (98 mL) and the mixture was stirred for 12 h to ensure soaking/exchange. After water exchange or soaking step, the leaves were filtered off and quickly cut into smaller pieces (*ca.* 1 × 1 mm) to allow more efficient diffusion of titanium isopropoxide within the leaf structure. Titanium isopropoxide (1.8 mL, 6.5 mmol) was then added using a syringe to the suspension of dry leaves (stirred at 250 rpm) in dry isopropanol (98 mL) as sol–gel precursor. The mixture was kept stirring at room temperature for another 12 h. Finally, the mixture was refluxed with stirring for 6 h, cooled and the product was filtered off, washed with isopropanol (10 mL), and dried in an aerated oven at 353 K for 12 h. The sample was then heat treated under static air at 773 K for 2 h (ramping rate of 1 K min^{-1} to avoid thermal shock damage) to remove all organic components and to crystallize the TiO$_2$ leaves.

Intact chloroplasts were isolated from *Spinacia oleracea* leaves using the method proposed by Robinson *et al.*[39] as described in Scheme S1.† The resulted chloroplast cells were used as biotemplates for the replication of the nanostructure of leaf photosystem using the abovementioned Ti^{3+} exchange method with no cutting of leaves required. The product was filtered off, washed with isopropoxide, dried and heat treated at 773 K for 2 h (ramping rate of 1 K min^{-1}) under static air.

2.3 Characterization

The morphology of the TiO$_2$ architectures synthesized *via* the bio-templating method was imaged using a JEOL 7000F scanning electron microscope (SEM). The samples were sputtered with carbon, and the working distance was varied between 10 mm and 4 mm to give the best image quality; the accelerating voltage was maintained at 10 kV.

Transmission electron microscopy (TEM) images were recorded using a Philips CM-200 transmission electron microscope operating at 200 kV. The samples were prepared by sonication in ethanol until fully dispersed followed by drop-casting onto a 150 square mesh copper TEM grid coated with carbon film.

The crystal phase of TiO$_2$ was identified by X-ray diffraction (XRD) on a Bruker APEXII X-ray diffractometer equipped with a Mo Kα radiation source and a graphite monochromator.

The surface area was estimated by nitrogen adsorption measurements using the BET equation. The measurements were conducted at 77 K using a Micromeritics Gemini VI 2385-C Surface Area Analyser. All of the samples were degassed at 473 K under vacuum overnight before the measurements.

The surface compositions were measured by X-ray photoelectron spectroscopy (XPS) using a Thermo Scientific ESCA-LAB250Xi probe with monochromated Al Kα radiation ($h\nu$ = 1486.68 eV). The binding energy was calibrated using the C 1s peak at 284.8 eV as reference. Measured spot was defined as a 500 μm square. The survey scans and the high-resolution (HR) XPS spectra were collected at the pass energy of 100 eV and 20 eV, respectively, and the photoelectron take off angle at 90° with respect to the surface plane. The XPS data was analysed using the Avantage software.

Dynamic light scattering (DLS) measurements were performed using a Microtrak Zetatrak DLS instrument. The samples were homogeneously dispersed in Milli-Q water (1 g L^{-1}) *via* sonication for 15 min followed by 30 min of stirring (same conditions as used in the dye degradation reaction before UV/visible light irradiation) in order to evaluate of the particle size effect on the reaction.

2.4 Photocatalytic activity under UV and visible lights

Diffuse-reflectance UV-vis spectra were recorded using a Citra 4040 spectrophotometer equipped with an integrating sphere and operated in reflectance mode. The catalyst samples were diluted with BaSO$_4$, and the resulting mixture was uniformly mixed, ground and loaded into the sample-holder. UV-vis spectra were recorded in reflectance mode, and the obtained reflectance values (R) were transformed to the Kubelka–Munk function $F(R)$ according to the eqn (1):

$$F(R) = \frac{(1-R)^2}{2R} \tag{1}$$

The band gap was estimated by creating a Tauc plot of $(h\nu F(R))^{1/n}$ against $h\nu$ (where h is Planck's constant, ν is the frequency of vibration and $n = 1/2$ for direct transitions).[40]

The photocatalytic activity of the bio-mimicked TiO$_2$ architectures under ultraviolet (UV) and visible light was studied in methylene blue degradation in a batch mode. An enclosed photocatalytic chamber equipped with two 50 W LEDs with maximum intensities at 370 nm (UV), 440 nm (blue) or 515 nm (green) was used in these experiments with remote sampling performed using syringe equipped with a long needle. The light flux was monitored to ensure that it was consistent across all experiments. The experimental conditions were set according to the literature.[41–44] The solution pH was maintained at 7 to exclude the effects of acidity and alkalinity on the photocatalytic activity. The reaction solution was prepared by dispersing 15 mg

of catalyst in 100 mL of dye solution (6.5 mg of methylene blue in 1 L deionised water) in a clean, dry quartz tube. The slurry was sonicated for 15 min to ensure that the catalyst was homogeneously dispersed before the reaction. The dye-catalyst slurry in the quartz tube was placed into the sealed photolysis chamber and stirred for 30 min in the dark to reach adsorption equilibrium. A 3 mL initial sample was collected before irradiation started. The reaction was timed immediately after the irradiation began and the temperature of the solution increased only marginally (up to 303 K maximum) during irradiation. Samples were collected at different reaction time and were centrifuged twice (13 000 rpm, 3 min) and analysed by UV-vis spectroscopy within a wavelength range from 500 to 750 nm. The dye conversion was determined by eqn (2) on the basis of the maximum absorption.

$$\text{Conversion}\% = \frac{(A_0 - A_t)}{A_0} \times 100 \qquad (2)$$

where A_0 is the initial absorbance of dye and A_t is the absorbance at time t. The rate constants of the decolourization reaction was estimated using a pseudo first-order kinetic[45] (eqn (3)):

$$-\ln \frac{C_t}{C_0} = kt \qquad (3)$$

where C_0 is the initial concentration of dye, C_t is the concentration at time t, t is the irradiation time and k is the apparent kinetic constant. The total organic carbon (TOC) was measured using a Shimadzu (model TOC-L$_{CPH}$) TOC analyser.

Control experiments without irradiation were performed to make sure that adsorption equilibrium was established after 30 min. The result of the dark experiments are provided in Fig. S1.† Blank reactions were also conducted to ensure that the decomposition of methylene blue was due to the photocatalytic degradation. No significant dye conversion (<3%) was observed under UV and visible lights in the absence of photocatalyst. The result of blank reactions are included in the dye conversion figures.

The photocatalytic oxidation of ethanol was carried out in a stirred batch annular reactor made from quartz with an internal volume of 150 mL and wall thickness of 0.5 cm. The catalyst powder (50 mg) was suspended in 50 mL of 20 v/v% ethanol solution for typical batches. The reaction slurry was stirred vigorously at 500 rpm for 60 min using magnetic stirrer to ensure homogeneity before the reaction. The reactor was purged with an inert gas using Schlenk line technique and was closed tightly. The reactor was placed inside an enclosed photolysis chamber and the mixture was stirred at 250 rpm to prevent sedimentation of the catalyst. Green LEDs with a maximum intensity at 515 nm were used to irradiate the reactor. The solution temperature and the gas phase pressure were continuously monitored. A gas sample was collected at the end of each reaction using a gas-tight syringe (10 mL). The samples were immediately analysed using a gas chromatograph (SRI Instruments, methanizer FID and TCD detectors, Haysep-D column). The photocatalytic performance in ethanol oxidation was assessed by the CO$_2$ yield.

3 Results and discussion

3.1 Improved fabrication of the bio-templated TiO$_2$ leaf

The templated materials with micro- and nano-architecture of the leaf photosystem are referred to as a "micro- and nano-structure templated artificial leaf" (MNAL). The natural enzymatic reactions of chlorophyll breakdown generally include breakdown of the chlorophyll chains by the chlorophyllase enzyme, followed by the Mg-dechelatase step and then oxidation of pheophorbide.[46] In this study, the colour change of the acid treated leaves to the yellow-brown indicates the conversion of chlorophyll into pheophorbide.[47,48] The ion-exchange procedure was performed under inert atmosphere to prevent Ti^{3+} ions from oxidizing. Energy-dispersive X-ray spectroscopy (EDS) results in Table S1† clearly demonstrate that there are no detectable metal contents of Mg^{2+} and other metal ions present in the leaf template. This finding indicates that the acid treatment was effective in extracting such metals during the artificial leaf synthesis process. Trace amounts of a vast range of metals including Mg, Zn, Fe, Pb etc. were observed in the non-treated samples. The extraction of metal ions is significant because the presence of metals may affect the crystal phase formation of the final TiO$_2$ catalyst. In addition, the presence of metal ion impurities could make the final product composition difficult to control because the leaf contents change over the seasons.[49]

In this research, an important improvement of the synthesis method was made by a solvent exchange step using dry isopropanol. This step was introduced to exchange or extract water present within leaves and replace it with isopropanol and also washing out any remaining salts from ion-exchange procedure. Minimizing water content inside the leaves allows titanium isopropoxide to diffuse deep inside the leaves, allowing better replication of the structure. Attempts to perform extraction using Soxhlet technique resulted in visible structural deterioration of the leaves, most likely due to higher temperature of the process. It is well known that water is critically important for the start of titanium isopropoxide hydrolysis. Therefore, the sol–gel was carried out open to ambient air to allow very gradual diffusion of water into the system, which resulted in noticeable hydrolysis and formation of titania. When this step was performed under inert dry atmosphere (Ar, Schlenk line) no visible signs of titania sol formation can be detected, thus confirming success of the earlier water extraction step. Noteworthy, the optimum size of leaf cuts accelerate infiltration of titanium ions through the leaf structure. Preliminary experiments using larger sizes of leaf cuts (ca. 5 mm by 5 mm) produced material which had titania structures formed only at the periphery of the leaf fragments.

To investigate the relationship between the morphology of the bio-templated product and its photocatalytic performance, Ti^{3+} exchange step was excluded to produce templated materials with only the microstructure of leaf photosystem. According to Li et al.,[27] it is hypothesised that the Ti^{3+} ions get trapped within the thylakoids via ion-exchange with the hydrogen in the chlorophylls. During the heat treatment, the titania coat produced from titanium isopropoxide hydrolysis act as seeding sites for

crystallization of TiO_2 to form the nano-scale interconnected stacked-sheets structure. Hence, the sample synthesized *via* the sol–gel method alone does not possess the nano-architecture of leaf photosystem and is referred to as a "micro-structure mimicked artificial leaf" (MAL).

In our preliminary experiments, the sol–gel coating step of the Ti^{3+}-exchanged leaves was omitted to replicate the nano-architecture of leaf photosystem alone. The produced templated materials showed no photocatalytic activity for degradation of methylene blue under UV light which could be attributed to the titania crystalline phase. The XRD pattern of non-coated sample (Fig. S2†) shows that the crystalline phase is mostly rutile. These results show that eliminating of sol–gel step favours the anatase-to-rutile phase transformation during crystallization of the TiO_2 leaves. Therefore, intact chloroplast cells were isolated from *Spinacia oleracea* leaves using the method involving mechanical breaking of the cell wall and the plasma membrane, filtration of cell debris and unbroken leaf tissues, collection of chloroplasts by centrifugation, and separation of the intact chloroplasts from the broken ones. The resulted replicas of isolated chloroplast cells are referred to as "artificial chloroplast" (AChl).

Several samples from different synthesis batches were used to repeat the catalyst characterizations and photocatalytic activity experiments to ensure that the developed replication approach is reproducible. All characterizations were in an acceptable criteria and the photocatalytic activity results obtained from different batch of same catalysts under UV/visible light are within the error bars.

3.2 Catalyst characterization

Fig. 2a–c shows the scanning electron microscopy images of the final catalysts after calcination. These images demonstrate that the porous microstructures of the photosystem, including the palisade and spongy layers of the mesophylls, are replicated and the removal of the organic components of the leaves was successfully accomplished. The well-replicated layered nanostructures of the thylakoids in the chloroplast are shown in the higher resolution TEM images of the MNAL and AChl samples (Fig. 2d–f). The average length of the bio-templated TiO_2 chloroplasts is 1.5–2 μm, which is in a good agreement with the size of natural chloroplast cells.[50–52] The results show that the developed method provides a reliable approach to synthesize TiO_2 hierarchical architectures similar to natural materials. This improved templating method could address the issues in controlling the morphology of final product associated with conventional procedures of synthesis of TiO_2 structures.

The results of energy-dispersive X-ray spectroscopy (EDS) measurements summarized in Table S1† demonstrate that the templated materials are composed mostly from titanium and oxygen. Given a minimum of 2 wt% doping has been reported to be required to influence the efficiency of TiO_2 photocatalysts,[53] the trace amounts of other elements (N, P and C) retained within the synthesized catalysts from the biotemplates are considered insufficient to contribute to the photocatalytic performance of these materials. In addition, lack of detectable
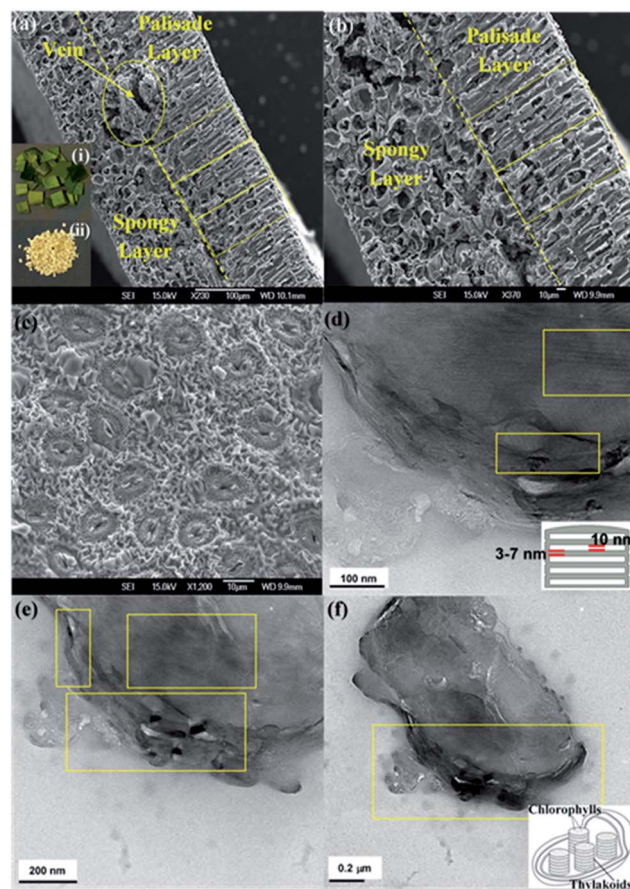

Fig. 2 (a and b) Cross-section SEM images of final catalysts, showing the well-replicated microarchitecture of the leaf photosystem. Inset: (i) photos of natural *camellia sinensis* leaves and (ii) TiO_2 artificial leaves. (c) Top-view SEM image of final catalysts, illustrating that the porous structure of the stomata is retained after the removal of the leaves. (d and e) TEM images of MNAL samples showing that the stack-layered nanostructures of the thylakoids in the chloroplast are retained after the removal of the leaves. (f) TEM images of AChl samples illustrating the well-replicated nano-architecture of the thylakoid membranes.

C within the templated samples based on the EDS analysis confirms the effective removal of the organic template which corroborates the observations made under SEM.

Although a mixture of anatase and rutile phases has been commonly reported for the room-temperature sol–gel synthesis of TiO_2 followed by a heat treatment, the phase formation strongly depends on several factors, including the nature and volume of the solution, the reaction atmosphere and time, the presences of impurities, the morphology of the sample, and also the rate and thermal homogeneity of the post-synthesis heat treatment.[54–56] The XRD patterns in Fig. 3 show that the MNAL and MAL consist predominantly of the anatase crystalline phase, whereas the AChl is a combination of anatase and rutile TiO_2 phases. The results show that our biotemplating method generally favours the formation of a pure anatase phase (the MNAL and MAL) after the samples underwent a heat treatment at 500 °C for 2 h under static air. This is consistent with the synthesis of TiO_2 films in which the initial crystalline TiO_2
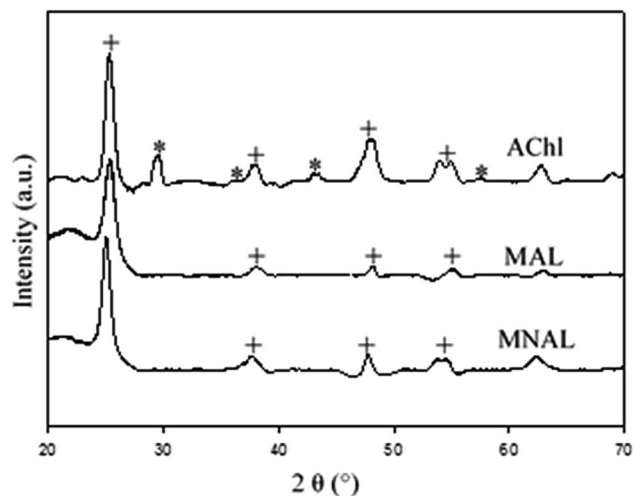
Fig. 3 XRD patterns of the final catalysts. Corresponding peaks of the anatase phase and the rutile phase TiO$_2$ are marked by "+" and "*", respectively.

Fig. 4 (a) General XPS spectrum of the MNAL and high resolution deconvoluted XPS spectra of (b) Ti 2p, (c) O 1s and (d) C 1s.

phase formed is usually anatase.[57,58] On the other hand, mixed phases of anatase and rutile in the AChl could be caused by a high ratio between the organic components from natural cells and TiO$_2$ during heat treatment. Many researches have attempted to study the effects of impurities on the anatase-to-rutile phase transformation. A high content of organic impurities can change the level of oxygen vacancies in the TiO$_2$ lattice, thus favouring the anatase to rutile phase transformation.[59] In addition, the faster phase transformation rate observed in the AChl also suggests that there are more potential nucleation sites available for the anatase-to-rutile transformation at low temperatures compared with the MNAL and MAL. As a result, the AChl is finely crystalline with small crystallite sizes.

Nitrogen (N$_2$) physisorption experiment shows that the specific surface area of the MAL and the MNAL are 29.9 m^2 g^{-1} and 66.1 m^2 g^{-1}, respectively (Fig. S3†). While both samples exhibited mesoporosity in their structures according to the hysteresis observed in the adsorption isotherms, MNAL specifically gave a H3 hysteresis loop indicating possible random pore network and irregular pore shape such as the "ink-bottle" geometry.[60] The stepwise desorption which occurred at the relative pressure of 0.55 suggests the characteristic desorption mechanism via cavitation and, thereby, confirms the presence of pore necks that are smaller than the critical size of N$_2$ (ca. 5–6 nm) at 77 K. In addition, the amount of N$_2$ adsorbed (mmol g^{-1}) on the MNAL is significantly higher than that adsorbed on the MAL (approximately 2.5 and 2.6 times higher on the MNAL at P/P_o of 0.3 and 0.9, respectively, as shown in Fig. S3†), demonstrating that the biotemplated nano-architecture derived from the thylakoid in chloroplasts present within the MNAL gives rise to a larger surface area.

The general XPS spectrum of the MNAL sample is shown in Fig. 4a. The P and Ca peaks centred at the binding energy (BE) of 133.7 and 347.7 eV could be assigned to the inorganic phosphate[61] and the calcium carbonate or phosphate species,[62] respectively. The small peak corresponding to N at BE of 400.1 eV could be attributed to the Ti nitride species.[63,64] The trace
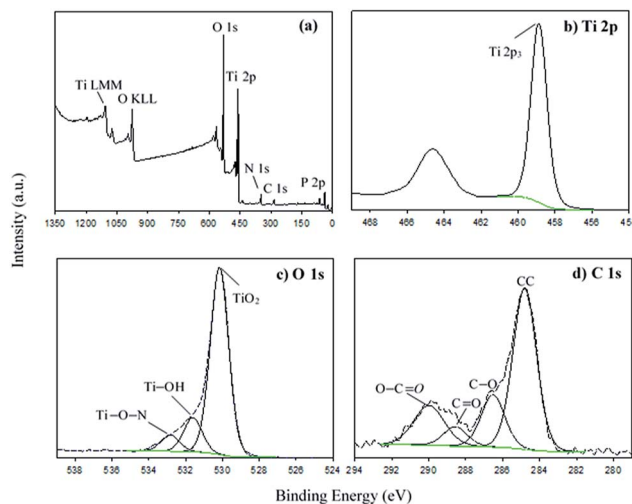
amounts of phosphorus, calcium and nitrogen detected in the MNAL sample are presumably residues remaining from the original biotemplate. The symmetric peak at the BE of 458.9 eV in the Ti 2p high resolution (HR) spectrum (Fig. 4b) is identified as TiO$_2$.[65,66] The BE for the Ti 2p peak is expected to decrease if chemical doping occurs, necessitating curve-fitting using peaks corresponding to several complex species.[63,67] However, in the MNAL sample only one symmetrical peak is observed, confirming that doping with other elements (N, C or P) is negligible. The HR spectrum of O 1s was deconvoluted using three peaks (Fig. 4c). From the reported TiO$_2$ models,[68,69] the first peak at the BE of 530.2 eV can be attributed to oxygen of the TiO$_2$ crystal lattice, the second at 531.6 eV can be attributed to the OH groups and the third one (BE = 532.8 eV) corresponds to Ti–O–N species.

Four carbon species with BE of 284.8 eV (A), 286.5 eV (B), 288.6 eV (C) and 290 eV (D) were observed in the C 1s spectrum (Fig. 4d). The species "A" and "B" could be assigned as carbon backbone (aromatic and aliphatic) and C–O bonds[70,71] within the adventitious carbon contaminants which are commonly reported in samples that have been exposed to the atmosphere.[65,71] The peaks "C" and "D" could be characteristic for the C=O and O–C=O groups due to the residual oxidized organic species of biotemplate, respectively.[71–73] Similar peaks were also observed in the C 1s spectra reported by Peng et al.[74] for the activated carbon derived from pomelo peel. Thus, carbon species "C" and "D" are probably related to the carbon species remaining after removal the leaf via calcination.[75,76]

No significant C content was detected in the bulk composition analysis by EDS (Table S1†), proving that the observed carbon species originated predominantly from contamination with adventitious carbon. The surface composition of the MNAL was specifically characterized because it exhibited the best photocatalytic performance among the three bio-templated samples both under UV (Fig. 5) and blue (Fig. 7) light. The elemental surface composition (atom%) of the MNAL is summarized in Table S2.†
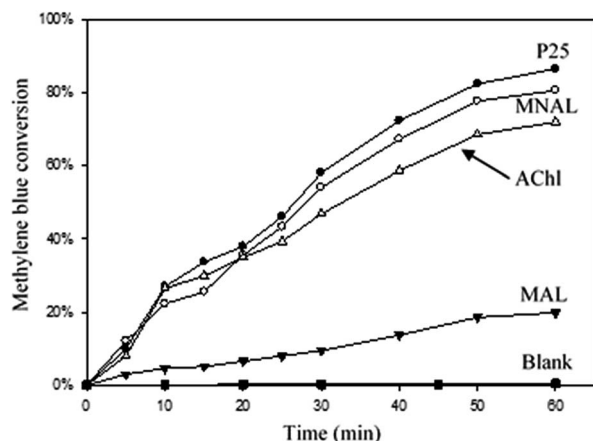
Fig. 5 Conversion of methylene blue under UV light with a maximum intensity at 370 nm. The experimental conditions are 6.5 ppm dye solution, a catalyst loading of 150 mg_{cat} L^{-1}, a pH of 7, 30 °C. The accuracy of all experiments was verified by series of repeated measurements and the relative error of less than 10% was determined.

3.3 Photocatalytic activity under UV and visible light

The efficiency of a photocatalytic reaction is an overall outcome of various factors: light absorption, transport of photogenerated charge carriers, electron/hole recombination rate and mass transfer of the reactant(s) or reactive radical species to/from the catalyst surface. The morphology of the photocatalyst, and particularly the particle size and shape, strongly influences the aforementioned factors.[77–79] Fig. 5 shows that the MNAL exhibited photocatalytic activity (80 ± 8%) comparable to that of the commercial P25 catalyst (86 ± 8.5%) after 60 min of irradiation under UV light (370 nm). The slightly higher conversion given by the commercial P25 (composed by approximately 80% anatase and 20% rutile) could be mainly due to the enhanced charge carrier transfer between anatase and rutile (preventing undesirable recombination) caused by the energy difference between the conduction band edges of the two phases.[80] On the other hand, nonporous TiO_2 catalysts are not capable of exhibiting favoured excitation behaviour in parallel with a high specific surface area, implying that photogenerated electron/hole pairs within the bulk of the semiconductor predominantly recombine before reaching the surface, causing a low quantum yield.[81–83]

In contrast to the nanoparticulate reference P25, prolonged residence time of the methylene blue within the internal interconnected membrane-like structures and unique hierarchical pore networks of MNAL could explain observed comparatively high activity. Thus, improved reactant-catalyst contact offsets the theoretically lower photocatalytic activity in the MNAL made of pure anatase phase, which is expected to have higher electron/hole recombination rates compared to P-25. In addition, Howe and Grätzel suggested that photoinduced charge carriers in TiO_2 nanomaterials can be efficiently trapped at different defect sites in the bulk and on the surface.[84,85] The electron/hole recombination rate could be reduced by providing charge traps at the defect sites located at

the surface of hierarchical structures MNAL TiO_2.[86–88] Here, we demonstrate that the structure that is responsible for the photocatalytic activity of the MNAL is the stacked titania nanosheets (thylakoid membranes replica) as the microarchitecture (palisade and spongy layers of the mesophylls) of the leaf photosystem tends to disintegrate under stirring. The DLS measurements showed that the synthesized MNAL and MAL catalysts break down to relatively small particles with an average diameter of 2.3 ± 0.2 μm during the reaction. The total organic carbon (TOC) measurement (Fig. S4†) shows that the commercial P25 and the MNAL catalysts decreased the TOC from 3.5 ± 0.2 to 2.5 ± 0.25 ppm (28.5 ± 3% decrease) and from 3.4 ± 0.2 to 2.7 ± 0.3 mg L^{-1} (20.5 ± 2% decrease), respectively. This is consistent with the results reported by Houas et al.[89] that the rate of mineralization of organic carbon by P25 TiO_2 is slow over the first hour of photocatalytic reaction despite fast decolourization of the dye. The TOC removal is expected to proceed further during a more prolonged reaction.

The AChl structures gave a slightly lower photocatalytic activity (72 ± 7% methylene blue conversion after 60 min) than the MNAL possibly due to insufficient mesoporous channels for fast adsorption and desorption of the reactants and oxidized products, respectively. This finding indicates that the porous structure, remaining from the broken mesophyll cells replica, could improve the photocatalytic activity. However, the light harvesting by the micro-architectures of the artificial leaf photosystem could not resemble that of the natural leaf due to structural breakdown in the slurry reaction system. Poor photocatalytic performance was observed in the case of using the MAL (only 20 ± 2% conversion) under UV light irradiation. This low activity in methylene blue degradation probably results from the low surface area of the MAL made of predominantly anatase crystalline phase; furthermore, nano-membrane structures (thylakoids replica) are absent in this catalyst. Moreover, the dye degradation measured for MAL (20%) after 120 min is 4 times lower than that measured for MNAL (80%). The difference in dye degradation efficiency is far greater than the 2.5-times factor due to the difference surface areas of these materials. The normalized results of photocatalytic degradation of methylene blue are presented in Table S3.† Both the MNAL and AChl catalysts exhibited photocatalytic dye degradation performance (34.7 and 31.2 mg g_{cat}^{-1}) similar to that of the nanoparticulate P25 (37.3 mg g_{cat}^{-1}) under UV light in contrast to the poor photocatalytic performance of the MAL (8.7 mg g_{cat}^{-1}). Thus, the layered nanostructures replicated from the thylakoid nanomembranes could be considered as the key contributing factor to the photocatalytic performance of the biotemplated materials under UV light.

Reported here easy multi-step chemical replication method for producing micro- and nanostructure-templated artificial leaves (MNAL) is better suited for large-scale synthesis compared with the AChl route relying on the isolation of intact chloroplast cells which yields only small quantity of material (average yield ∼ 40 mg chloroplasts per g spinach leaf[39,90]). Thus, the AChl was not included in the study of visible light activity. The diffuse-reflectance UV-vis spectra shown in Fig. 6 demonstrate two important features. Firstly, the MNAL exhibits
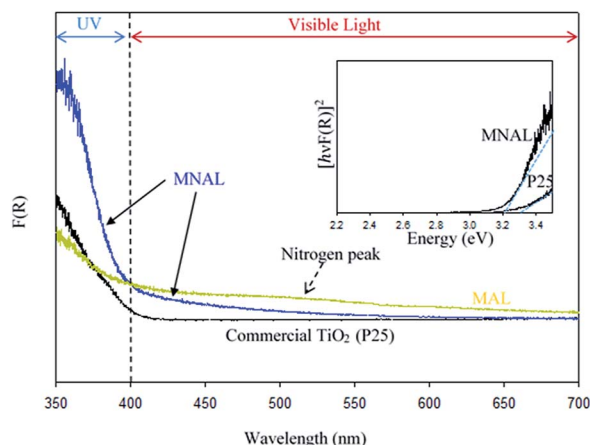
Fig. 6 Diffuse-reflectance UV-vis spectra of the MNAL, MAL and the reference P25 (inset: Tauc plot showing fits used for the estimation of band gap values; the MNAL spectrum was used to estimate the bandgap in order to exclude the effects from the nitrogen peak).
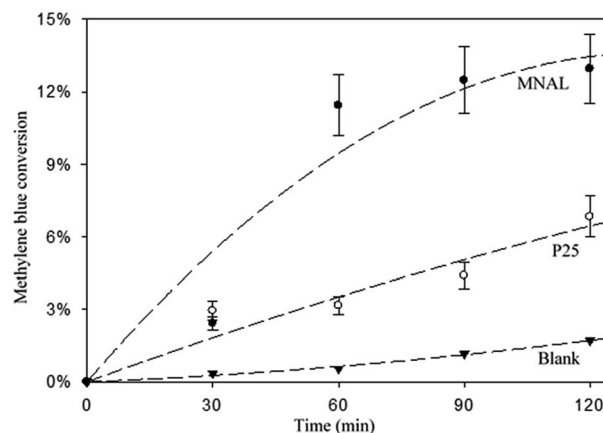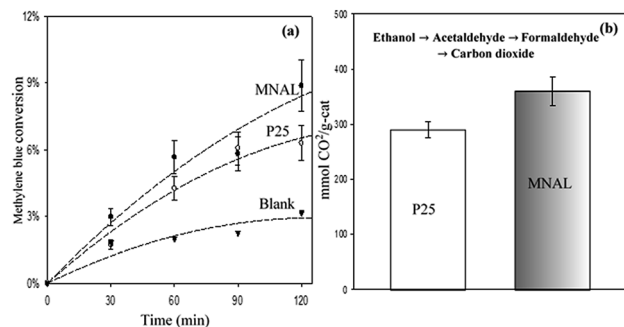

Fig. 7 Conversion of methylene blue under blue LEDs with a maximum intensity at 440 nm (the edge of the visible light region). The experimental conditions are 6.5 ppm dye solution, a catalyst loading of 150 mg$_{cat}$ L^{-1}, a pH of 7, 30 °C. Notes: (i) the MAL exhibited no photocatalytic activity under blue light (result not shown). (ii) A much lower conversion of methylene blue was recorded here due to the use of a lower energy light source; (iii) lines are guide to eyes.

greater absorption in the UV region over a broad UV-vis wavelength (*ca.* 350–600 nm) compared to the reference P25 material. We hypothesise that this is due to the improved light trapping and light scattering properties through the layered nano-architectures. Interestingly, this is consistent with the excellent light trapping properties of the parent biotemplating materials (*i.e.* natural chloroplasts) reported in literature,[35–37] which are capable of maximizing light scattering through the layered structures. Secondly, the absorption efficiency has been improved in the visible light region (particularly between 400–600 nm). Such improvement of the visible light absorbance can be attributed to the presence of localized states within the TiO$_2$ compact layers in the MNAL. There are two types of trap centres in TiO$_2$ nanostructures. First, the lattice defects, such as oxygen vacancies, that can form localised Ti^{3+} centres, which may lead to additional electronic states within the TiO$_2$ band gap, allowing sub-band gap transitions and thus light absorbance in the visible region. However, these were not observed in noticeable quantity in the XP spectra in this study. Second, higher surface area of such materials (66.1 m^2 g^{-1} in MNAL) may offer larger proportion Ti atoms at the surface which could act as trap centres, explaining improved light absorbance.[87,91] The advanced optical properties of titania nano-architectures have been observed by many research groups over the past few years.[14] For instance, Bavykin *et al.*[92] revealed the improved optical properties in TiO$_2$ nanotubes; Sato and Sakai *et al.* showed that the effective wavelengths for light harvesting red shifted when titania is fabricated in the form of nanosheets.[93,94]

The observed peak centred at *ca.* 500 nm in the spectrum of the MAL sample could be due to the absorption of light by N content.[95,96] However, the amount of N is insufficient to contribute to the photocatalytic efficiency of biotemplated catalyst as discussed earlier. There is no detectable absorption peak associated with N content in the MNAL spectrum, suggesting that the amount of nitrogen in the catalyst retained from the leaf is negligible (corroborating results in Table S1†).

This shows that the extrinsic excitation behaviour of TiO$_2$ photocatalyst can potentially be augmented by modifying its morphology without changing its composition. The Tauc plot in Fig. 6 (inset) allows to roughly estimate an energy band gap of 3.2 eV for the MNAL, which is lower than that of the reference P25 TiO$_2$ (E_g = 3.3 eV). Although only a minor reduction of bandgap is evidenced by the Tauc plot, the result is in good agreement with reported band gap narrowing by only 0.2 eV *via* structural modification for TiO$_2$ nanomaterials.[97]

The results of the methylene blue photo-degradation in Fig. 7 and 8a show that the MNAL gave a significantly better photocatalytic activity than P25 under both visible blue and green lights. MNAL and P25 achieved 13 ± 1.5% and 7 ± 0.9% of methylene blue conversion, respectively, under blue light at 440 nm which is near the edge of the visible region (Fig. 7). Under green light irradiation at 515 nm (Fig. 8a), the methylene blue conversion achieved by MNAL (9 ± 1.2%) is also higher than that achieved by P25 (6.3 ± 0.8%). In addition, the MAL exhibited no apparent photocatalytic activity in methylene blue degradation under blue light (not shown here). The improved visible-light activity of the MNAL could be attributed to several key factors, large surface area and high efficiency of light absorption provided by the morphology of the chloroplast-like structures (see earlier discussion of UV-vis spectra). We hypothesise that the 3-D TiO$_2$ nanocrystalline structure of the MNAL allows rapid injection of charge carriers from bulk into both internal and external surfaces. One of the carriers is then captured on a localised state at the surface while the other one is free for reaction. The net result is that the electron/hole recombination rate is reduced significantly by both the 3-D layered structure and the charge trapping phenomena resulted from defect points located within the volume of the MNAL. The 3-D construction of the interconnected nanolayers (replicated from thylakoids) in the MNAL also allows efficient trapping of the incident light *via*

Fig. 8 (a) Conversion of methylene blue under green LEDs with a maximum intensity at 515 nm. The experimental conditions are 6.5 ppm dye solution, a catalyst loading of 150 mg_{cat} L^{-1}, a pH of 7, 30 °C (note: lines are guide to eyes). (b) Carbon dioxide yield of photocatalytic oxidation of ethanol under green LEDs with a maximum intensity at 515 nm. The experimental conditions are 20 v/v% ethanoic solution, a catalyst loading of 1 g_{cat} L^{-1}, 30 °C.

multiple light scattering within structure of MNAL. Thus, a longer optical path[35–37] of light travelling through MNAL could result in the greater chance of the eventual photoexcitation events during the photocatalytic reaction. This is consistent with other reported results on the 3-D crystalline materials.[25,98,99] For example, Cheng et al.[24] showed a high photocurrent density of 3-D TiO_2 inverse opals under simulated solar-light illumination. Attempts to measure the TOC removal under blue and green lights were not successful owing to low conversion of methylene blue under the tested conditions. The change in TOC concentration was very small after 2 h of reaction under visible lights and was within the uncertainty of the TOC measurement.

The apparent rate constants are estimated using data reported in Fig. S5.† The MNAL catalyst gave a rate constant approximately 2.4 and 1.3 times higher than those observed in the case of P25 under blue and green light irradiation, respectively (Fig. S5b and c†). Given that nitrogen species were evidenced by EDS and XPS analysis (Tables S1 and S2†), the estimated rate constants are also compared with the rate constant given by N-doped TiO_2 in the work of Burda et al.[100] Burda et al. reported that the rate constants of methylene blue photo-degradation by N-doped TiO_2 (8 atomic%) are approximately 3 and 1.5 times higher than those given by the benchmark P25 titania under near blue (390 nm) and green (540 nm) light irradiation, respectively. The superior visible-light photocatalytic activity in heavily N-doped TiO_2 compared with the MNAL could be attributed to the band gap narrowing of titania resulting from substitution of O for N in the TiO_2 lattice. As stated earlier in the discussion of the XPS spectra, the amount of N dopant observed in this work is insufficient to form localized centres by mixing N 1s states with O 1s states in the MNAL. Hence, the trace amount of N dopant is less likely to have influence on the photocatalytic activity of the MNAL.

Photocatalytic oxidation of ethanol (Fig. 8b) was also conducted as an alternative probe reaction to verify the superior photocatalytic activity of MNAL under green light (515 nm). Ethanol oxidation on TiO_2 catalysts are initiated by oxidizing the adsorbed ethanol molecules to acetaldehyde and proceed through

several intermediate reactions.[101] The results show that the yield of CO_2 generated by MNAL (360 $\pm$ 25 μmol g_{cat}^{-1}) is almost 1.3 times higher than the yield of CO_2 given by P25 (290 $\pm$ 15 μmol g_{cat}^{-1}) under green light. The MNAL was specifically tested against the reference TiO_2 under green light because it gave the best photocatalytic performance among the three bio-templated samples under UV and blue wavelengths (as shown in Fig. 5 and 7). The electron transfer from rutile crystals to the trapping sites of anatase lattice extends the light absorption efficiency of P25 into visible range.[80] On the other hand, the pure anatase (single crystalline phase) with a crystalline domain diameter below the critical radius of approximately 10 nm may exhibit an increase in band gap, causing low photocatalytic efficiency under the visible light.[102,103] We demonstrate that sub-band gap transitions caused by the localized states within the compact, layered nanostructure in the MNAL could lead to a stable charge separation over a broad range of visible wavelengths, despite its pure anatase phase. The detailed mechanisms of the photocatalytic oxidation of ethanol over the biotemplated MANL titania will be examined further in our follow-up study.

4 Conclusions

In this study, we developed a multi-step chemical replication method using micro- to nano-architectures of the green leaves as templates to prepare advanced visible-light active TiO_2-based photocatalyst. Novel micro- and nano-structured porous pure anatase-based architecture enabled by biotemplating (MNAL) exhibited photocatalytic dye degradation performance similar to that of commercial nanoparticulate mixed-phase P25 catalyst under UV light. A substantially improved photocatalytic activity was observed with the MNAL under visible (blue and green) light. The enhanced photocatalytic performance of the MNAL was interpreted as arising due to the complex 3-D morphology of the templated macro- and nano-structured light-harvesting system. This catalyst contains extensive pore network and has high surface area resulting from the interconnected titania nanosheets derived from the thylakoid membranes of the natural leaves. This work demonstrated that the extrinsic excitation behaviour of TiO_2 photocatalyst can be potentially augmented by modifying its morphology alone. The synthesis method reported in this work provides a reliable and promising procedure to synthesize TiO_2 hierarchical structures which could overcome the issues in controlling the structure and crystallinity of end product associated with conventional procedures. The unique advantages of the layered TiO_2 structure made using biotemplating method are confirmed by the performance of reported here materials in two model photocatalytic reactions under visible light. Given that visible light with wavelengths longer than 400 nm makes up more than 95% of the solar spectrum, the novel TiO_2 structure obtained using biotemplating method could be extremely attractive for solar-assisted chemical reactions.

Conflicts of interest

There are no conflicts of interest to declare.

Acknowledgements

References

1 D. Abbott, *Proc. IEEE*, 2010, **98**, 42–66.

2 S. C. Roy, O. K. Varghese, M. Paulose and C. A. Grimes, *ACS Nano*, 2010, **4**, 1259–1278.

3 E. B. Stechel and J. E. Miller, *J. CO$_2$ Util.*, 2013, **1**, 28–36.

4 A. Corma and H. Garcia, *J. Catal.*, 2013, **308**, 168–175.

5 K. Mori, H. Yamashita and M. Anpo, *RSC Adv.*, 2012, **2**, 3165–3172.

6 G. Liu, L. Wang, H. G. Yang, H.-M. Cheng and G. Q. Lu, *J. Mater. Chem.*, 2010, **20**, 831–843.

7 M. Kitano, M. Matsuoka, M. Ueshima and M. Anpo, *Appl. Catal., A*, 2007, **325**, 1–14.

8 E. Serrano, G. Rus and J. García-Martínez, *Renewable Sustainable Energy Rev.*, 2009, **13**, 2373–2384.

9 M. Woodhouse and B. A. Parkinson, *Chem. Soc. Rev.*, 2009, **38**, 197–210.

10 M. Gao, L. Zhu, W. L. Ong, J. Wang and G. W. Ho, *Catal. Sci. Technol.*, 2015, **5**, 4703–4726.

11 B. Liu, Y. Fang, Z. Li and S. Xu, *J. Nanosci. Nanotechnol.*, 2015, **15**, 889–920.

12 S. Khanchandani, S. Kumar and A. K. Ganguli, *ACS Sustainable Chem. Eng.*, 2016, **4**, 1487–1499.

13 B. Sarkar, N. Singhal, R. Goyal, A. Bordoloi, L. N. Sivakumar Konathala, U. Kumar and R. Bal, *Catal. Commun.*, 2016, **74**, 43–48.

14 X. Chen and S. S. Mao, *Chem. Rev.*, 2007, **107**, 2891–2959.

15 D. P. MacWan, P. N. Dave and S. Chaturvedi, *J. Mater. Sci.*, 2011, **46**, 3669–3686.

16 A. Chen, J. Qian, Y. Chen, X. Lu, F. Wang and Z. Tang, *Powder Technol.*, 2013, **249**, 71–76.

17 P. H. Mutin and A. Vioux, *Chem. Mater.*, 2009, **21**, 582–596.

18 H. G. Yang, C. H. Sun, S. Z. Qiao, J. Zou, G. Liu, S. C. Smith, H. M. Cheng and G. Q. Lu, *Nature*, 2008, **453**, 638–641.

19 J.-Y. Ruzicka, F. A. Bakar, L. Thomsen, B. C. Cowie, C. McNicoll, T. Kemmitt, H. E. A. Brand, B. Ingham, G. G. Andersson and V. B. Golovko, *RSC Adv.*, 2014, **4**, 20649–20658.

20 C. Sanchez, H. Arribart and M. M. Giraud Guille, *Nat. Mater.*, 2005, **4**, 277–288.

21 F. Xia and L. Jiang, *Adv. Mater.*, 2008, **20**, 2842–2858.

22 A. H. Lu and F. Schüth, *Adv. Mater.*, 2006, **18**, 1793–1805.

23 H. Zhou, T. Fan and D. Zhang, *ChemSusChem*, 2011, **4**, 1344–1387.

24 C. Cheng, S. K. Karuturi, L. Liu, J. Liu, H. Li, L. T. Su, A. I. Y. Tok and H. J. Fan, *Small*, 2012, **8**, 37–42.

25 G. I. N. Waterhouse and M. R. Waterland, *Polyhedron*, 2007, **26**, 356–368.

26 X. H. Li, W. M. Liu and H. L. Li, *Appl. Phys. A*, 2005, **80**, 317–320.

27 X. Li, T. Fan, H. Zhou, S. K. Chow, W. Zhang, D. Zhang, Q. Guo and H. Ogawa, *Adv. Funct. Mater.*, 2009, **19**, 45–56.

28 X. Ye, Q. Yang, Y. Zheng, W. Mo, J. Hu and W. Huang, *Mater. Res. Bull.*, 2014, **51**, 366–371.

29 A. Chen, J. Qian, Y. Chen, X. Lu, F. Wang and Z. Tang, *Powder Technol.*, 2013, **249**, 71–76.

30 Ü. Niinemets and L. Sack, in *Progress in Botany*, ed. K. Esser, U. Lüttge, W. Beyschlag and J. Murata, Springer, Berlin, Heidelberg, 2006, pp. 385–419.

31 R. A. Bone, D. W. Lee and J. M. Norman, *Appl. Opt.*, 1985, **24**, 1408–1412.

32 M. E. Poulson and T. C. Vogelmann, *Plant, Cell Environ.*, 1990, **13**, 803–811.

33 T. C. Vogelmann and G. Martin, *Plant, Cell Environ.*, 1993, **16**, 65–72.

34 T. C. Vogelmann, J. F. Bornman and D. J. Yates, *Physiol. Plant.*, 1996, **98**, 43–56.

35 L. Mustárdy, *Oxygenic Photosynthesis: The Light Reactions*, Kluwer, Dordrecht, Netherlands, 1996.

36 A. V. Ruban, M. P. Johnson and C. D. P. Duffy, *Energy Environ. Sci.*, 2011, **4**, 1643–1650.

37 I. Rumak, K. Gieczewska, B. Kierdaszuk, W. I. Gruszecki, A. Mostowska, R. Mazur and M. Garstka, *Biochim. Biophys. Acta, Bioenerg.*, 2010, **1797**, 1736–1748.

38 Z. He, W. Que and Y. He, *Mater. Lett.*, 2013, **94**, 136–139.

39 S. P. Robinson, *Photosynth. Res.*, 1983, **4**, 281–287.

40 S. Adachi, *Optical Properties of Crystalline and Amorphous Semiconductors*, Kluwer, Norwell MA, 1999.

41 R. J. Tayade, T. S. Natarajan and H. C. Bajaj, *Ind. Eng. Chem. Res.*, 2009, **48**, 10262–10267.

42 F. Abu Bakar, J.-Y. Ruzicka, I. Nuramdhani, B. E. Williamson, M. Holzenkaempfer and V. B. Golovko, *Aust. J. Chem.*, 2015, **68**, 471–480.

43 S. Bae, S. Kim, S. Lee and W. Choi, *Catal. Today*, 2014, **224**, 21–28.

44 J. Yao and C. Wang, *Int. J. Photoenergy*, 2010, 643182.

45 X. Yan, C. Zou, X. Gao and W. Gao, *J. Mater. Chem.*, 2012, **22**, 5629–5640.

46 S. Hörtensteiner and B. Kräutler, *Biochim. Biophys. Acta, Bioenerg.*, 2011, **1807**, 977–988.

47 A. Drzewiecka-Matuszek, A. Skalna, A. Karocki, G. Stochel and L. Fiedor, *J. Biol. Inorg Chem.*, 2005, **10**, 453–462.

48 H. Küpper, F. Küpper and M. Spiller, *Photosynth. Res.*, 1998, **58**, 123–133.

49 J. Yuan, D. Yuan, X. Tan, F. Zou and S. Xiao, *Open Biotechnol. J.*, 2015, **9**, 170–177.

50 J. R. Ellis and R. M. Leech, *Planta*, 1985, **165**, 120–125.

51 Ł. Rudowska, K. Gieczewska, R. Mazur, M. Garstka and A. Mostowska, *Biochim. Biophys. Acta, Bioenerg.*, 2012, **1817**, 1380–1387.

52 E. Shimoni, O. Rav-Hon, I. Ohad, V. Brumfeld and Z. Reich, *Plant Cell*, 2005, **17**, 2580–2586.

53 S. Rehman, R. Ullah, A. M. Butt and N. D. Gohar, *J. Hazard. Mater.*, 2009, **170**, 560–569.

54 S. D. Sharma, D. Singh, K. K. Saini, C. Kant, V. Sharma, S. C. Jain and C. P. Sharma, *Appl. Catal., A*, 2006, **314**, 40–46.

55 Y. Takahashi and Y. Matsuoka, *J. Mater. Sci.*, 1988, **23**, 2259–2266.

56 N. Smirnova, A. Eremenko, V. Gayvoronskij, I. Petrik, Y. Gnatyuk, G. Krylova, A. Korchev and A. Chuiko, *J. Sol-Gel Sci. Technol.*, 2004, **32**, 357–362.

57 K. Okada, N. Yamamoto, Y. Kameshima, A. Yasumori and K. J. D. MacKenzie, *J. Am. Ceram. Soc.*, 2001, **84**, 1591–1596.

58 H. Shin, H. S. Jung, K. S. Hong and J.-K. Lee, *J. Solid State Chem.*, 2005, **178**, 15–21.

59 D. A. H. Hanaor and C. C. Sorrell, *J. Mater. Sci.*, 2011, **46**, 855–874.

60 K. Sing and R. Williams, *Adsorpt. Sci. Technol.*, 2004, **22**, 773–782.

61 S. Caporali, U. Bardi and A. Lavacchi, *J. Electron Spectrosc. Relat. Phenom.*, 2006, **151**, 4–8.

62 Z. Zhao, W. Shan, Y. Zhang, X. Li, J. Ma and Y. Yan, *J. Appl. Polym. Sci.*, 2012, **125**, 2502–2509.

63 Y. Cong, J. Zhang, F. Chen and M. Anpo, *J. Phys. Chem. C*, 2007, **111**, 6976–6982.

64 G. A. Battiston, R. Gerbasi, A. Gregori, M. Porchia, S. Cattarin and G. A. Rizzi, *Thin Solid Films*, 2000, **371**, 126–131.

65 P. Górska, A. Zaleska, E. Kowalska, T. Klimczuk, J. W. Sobczak, E. Skwarek, W. Janusz and J. Hupka, *Appl. Catal., B*, 2008, **84**, 440–447.

66 N. Drnovšek, N. Daneu, A. Rečnik, M. Mazaj, J. Kovač and S. Novak, *Surf. Coat. Technol.*, 2009, **203**, 1462–1468.

67 M. Paszkiewicz, J. Łuczak, W. Lisowski, P. Patyk and A. Zaleska-Medynska, *Appl. Catal., B*, 2016, **184**, 223–237.

68 E. György, A. Pérez del Pino, P. Serra and J. L. Morenza, *Surf. Coat. Technol.*, 2003, **173**, 265–270.

69 J. Yu, X. Zhao and Q. Zhao, *Thin Solid Films*, 2000, **379**, 7–14.

70 G. Xue, Q. Dai and S. Jiang, *J. Am. Chem. Soc.*, 1988, **110**, 2393–2395.

71 J. J. Lagowski, *J. Chem. Educ.*, 1993, **70**, A25.

72 L. Calliari, S. Fanchenko and M. Filippi, *Carbon*, 2007, **45**, 1410–1418.

73 G. Milczarek, A. Ciszewski and I. Stepniak, *J. Power Sources*, 2011, **196**, 7882–7885.

74 C. Peng, J. Lang, S. Xu and X. Wang, *RSC Adv.*, 2014, **4**, 54662–54667.

75 J. Chen, G. Zhang, B. Luo, D. Sun, X. Yan and Q. Xue, *Carbon*, 2011, **49**, 3141–3147.

76 J.-w. Lang, X.-b. Yan, W.-w. Liu, R.-t. Wang and Q.-j. Xue, *J. Power Sources*, 2012, **204**, 220–229.

77 H. Cheng, J. Wang, Y. Zhao and X. Han, *RSC Adv.*, 2014, **4**, 47031–47038.

78 A. Testino, I. R. Bellobono, V. Buscaglia, C. Canevali, M. D'Arienzo, S. Polizzi, R. Scotti and F. Morazzoni, *J. Am. Chem. Soc.*, 2007, **129**, 3564–3575.

79 M. Schiavello, *Heterogeneous Photocatalysis*, Wiley, 1997, pp. 117–125.

80 D. C. Hurum, A. G. Agrios, K. A. Gray, T. Rajh and M. C. Thurnauer, *J. Phys. Chem. B*, 2003, **107**, 4545–4549.

81 H. Lin, C. P. Huang, W. Li, C. Ni, S. I. Shah and Y.-H. Tseng, *Appl. Catal., B*, 2006, **68**, 1–11.

82 W. C. Hao, S. K. Zheng, C. Wang and T. M. Wang, *J. Mater. Sci. Lett.*, 2002, **21**, 1627–1629.

83 J. Jiang, G. Oberdörster, A. Elder, R. Gelein, P. Mercer and P. Biswas, *Nanotoxicology*, 2008, **2**, 33–42.

84 R. F. Howe and M. Grätzel, *J. Phys. Chem.*, 1985, **89**, 4495–4499.

85 R. F. Howe and M. Grätzel, *J. Phys. Chem.*, 1987, **91**, 3906–3909.

86 M. K. Nowotny, L. R. Sheppard, T. Bak and J. Nowotny, *J. Phys. Chem. C*, 2008, **112**, 5275–5300.

87 R. Krishnan, in *Encyclopedia of Electrochemistry*, Wiley, 2007, vol. 6, pp. 34–39.

88 I. R. Macdonald, S. Rhydderch, E. Holt, N. Grant, J. M. D. Storey and R. F. Howe, *Catal. Today*, 2012, **182**, 39–45.

89 A. Houas, H. Lachheb, M. Ksibi, E. Elaloui, C. Guillard and J.-M. Herrmann, *Appl. Catal., B*, 2001, **31**, 145–157.

90 M. Nishimura, D. Graham and T. Akazawa, *Plant Physiol.*, 1976, **58**, 309–314.

91 I. Abayev, A. Zaban, V. G. Kytin, A. A. Danilin, G. Garcia-Belmonte and J. Bisquert, *J. Solid State Electrochem.*, 2007, **11**, 647–653.

92 D. V. Bavykin, S. N. Gordeev, A. V. Moskalenko, A. A. Lapkin and F. C. Walsh, *J. Phys. Chem. B*, 2005, **109**, 8565–8569.

93 N. Sakai, Y. Ebina, K. Takada and T. Sasaki, *J. Am. Chem. Soc.*, 2004, **126**, 5851–5858.

94 H. Sato, K. Ono, T. Sasaki and A. Yamagishi, *J. Phys. Chem. B*, 2003, **107**, 9824–9828.

95 R. Asahi, T. Morikawa, T. Ohwaki, K. Aoki and Y. Taga, *Science*, 2001, **293**, 269–271.

96 K. Yang, Y. Dai and B. Huang, *J. Phys. Chem. C*, 2007, **111**, 12086–12090.

97 V. Etacheri, C. Di Valentin, J. Schneider, D. Bahnemann and S. C. Pillai, *J. Photochem. Photobiol., C*, 2015, **25**, 1–29.

98 G. I. N. Waterhouse, J. B. Metson, H. Idriss and D. Sun-Waterhouse, *Chem. Mater.*, 2008, **20**, 1183–1190.

99 I. Paramasivam, H. Jha, N. Liu and P. Schmuki, *Small*, 2012, **8**, 3073–3103.

100 C. Burda, Y. Lou, X. Chen, A. C. S. Samia, J. Stout and J. L. Gole, *Nano Lett.*, 2003, **3**, 1049–1051.

101 D. S. Muggli, J. T. McCue and J. L. Falconer, *J. Catal.*, 1998, **173**, 470–483.

102 K. Kočí, L. Obalová, L. Matějová, D. Plachá, Z. Lacný, J. Jirkovský and O. Šolcová, *Appl. Catal., B*, 2009, **89**, 494–502.

103 S. M. Gupta and M. Tripathi, *Chin. Sci. Bull.*, 2011, **56**, 1639–1657.